Final Technical Report

Federal grant DE-SC0010730

Experimental and numerical investigation of reactive shock-accelerated flows

Principal Investigator: Riccardo Bonazza, 608-265-2337, bonazza@engr.wisc.edu

Submitted: December 20, 2016

University of Wisconsin-Madison

Department of Engineering Physics, 1500 Engineering Dr., Madison, WI 53706

Grant Period: 9/1/2013-8/31/2016

1 Abstract

2 Objectives

The main goal of this program was to establish a qualitative and quantitative connection, based on the appropriate dimensionless parameters and scaling laws, between shock-induced distortion of astrophysical plasma density clumps and their earthbound analog in a shock tube.

These objectives were pursued by carrying out laboratory experiments and numerical simulations to study the evolution of two gas bubbles accelerated by planar shock waves and compare the results to available astrophysical observations. The experiments were carried out in an vertical, downward-firing shock tube, 9.2 m long, with square internal cross section (25×25 cm^2). Specific goals were to quantify the effect of the shock strength (Mach number, M) and the density contrast between the bubble gas and its surroundings (usually quantified by the Atwood number, $A \equiv \frac{\rho_1 - \rho_2}{\rho_1 + \rho_2}$, where ρ_1 and ρ_2 are the densities of the two gases) upon some of the most important flow features (*e.g.* macroscopic properties; turbulence and mixing rates).

The computational component of the work performed through this program was aimed at (a) studying the physics of multi-phase compressible flows in the context of astrophysics plasmas and (b) providing a computational connection between laboratory experiments and the astrophysical application of shock-bubble interactions.

Throughout the study, we used the `FLASH`4.2 [1] code to run hydrodynamical and magnetohydrodynamical simulations of shock bubble interactions (SBI) on an adaptive mesh.

3 Experiments

A schematic of the vertical shock tube facility and views of the driver and test sections are shown in Figs. 3(a) and (b), respectively. A detailed description of the apparatus is given in [2].

The shock tube is downward-firing, with a large (25×25 cm^2) square inner cross section, and approximately 9 m long. The square internal cross section provides the parallel walls necessary for flow visualization without resorting to a structurally weak tube extension.

The driver section is at the top of the shock tube. A shock wave is generated by rupturing a steel diaphragm by pressurizing the driver section above the diaphragm structural limit. To achieve this, before each experiment, the driver section is pressurized to about 90% of the diaphragm rupture limit. Two gas cylinders at about 200 bar are connected to the driver section via fast-opening valves. To initiate an experiment, the valves are opened, the pressure in the driver rises quickly above the rupture limit, and the diaphragm breaks. This procedure allows tight control of the time of shock release (with an uncertainty less than 200 ms).

In a typical experiment, a pair of gas bubbles (either Ar-Ar or Xe-Ar) are released in free fall in a nitrogen environment and a downward-traveling, planar shock wave with Mach number M=1.47 impulsively accelerates the bubbles. A new dual injector system was designed and fabricated in the first year of the program. The new system consists of two injectors that retract by sliding horizontally across the shock

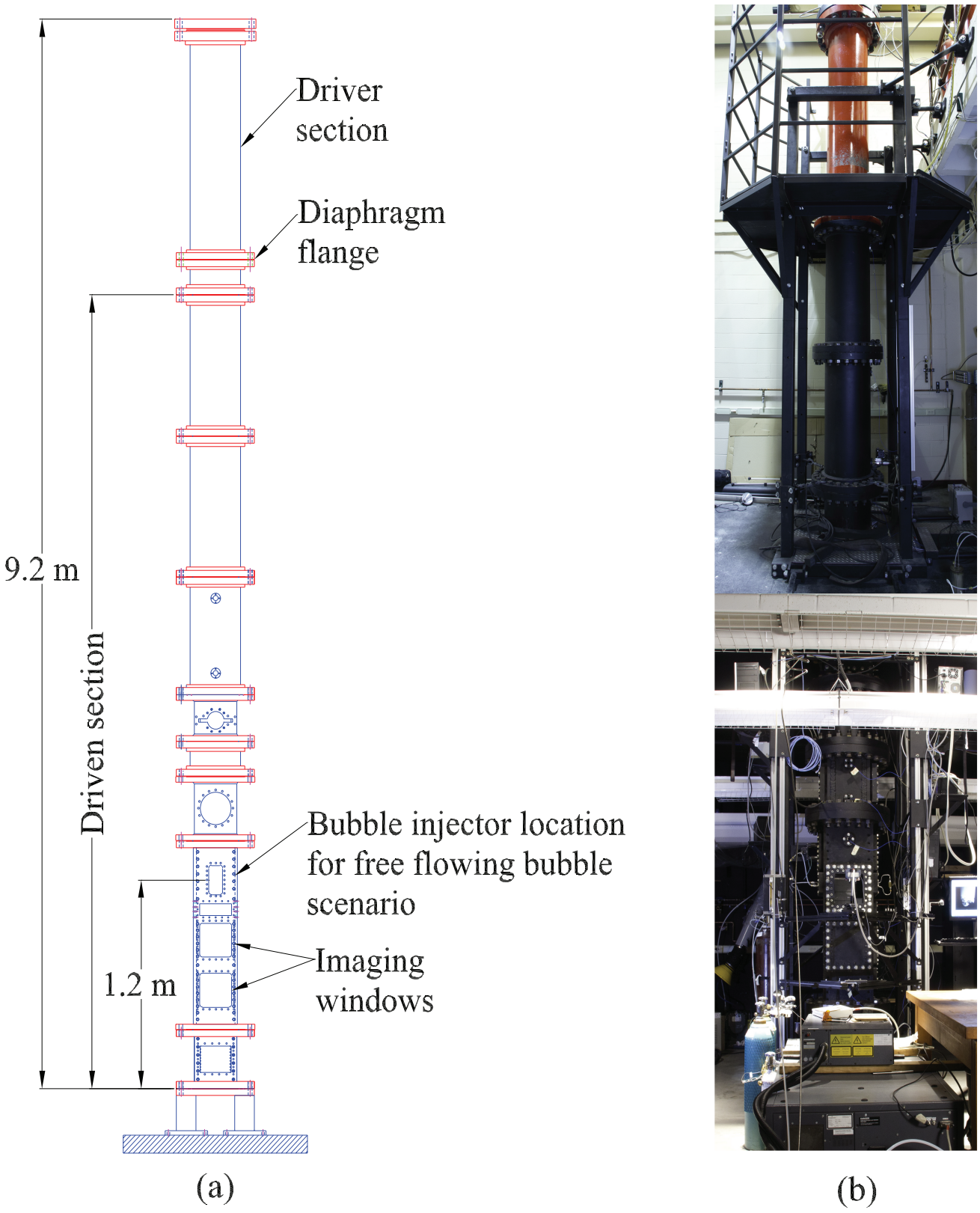

Figure 1: Vertical shock tube: (a) schematic; (b) views of driver and test sections.

tube wall, terminating their run with their heads flush with the inner wall surface. A schematic of the dual injector is shown in Fig. 2.

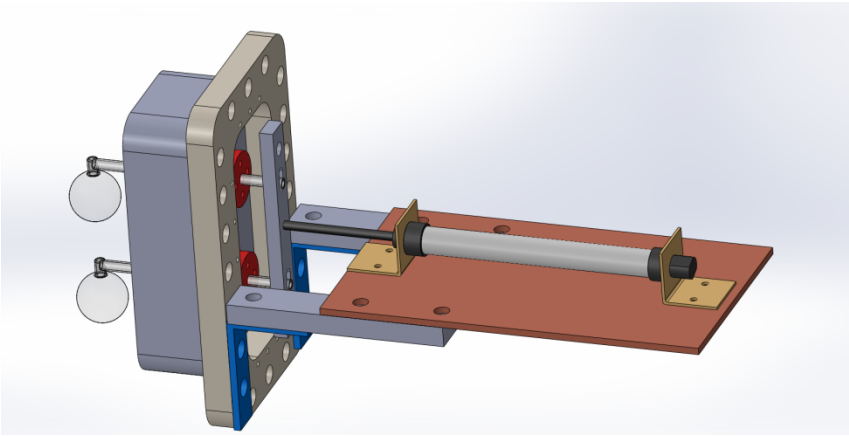

Figure 2: Schematic view of the double injector system.

The new configuration was dictated by the need to have the two bubbles vertically lined up at the time of their release into the shock tube. Figure 3 shows a typical injector retraction sequence. While the sideways retraction does impart a small rotation rate onto the bubbles, this appears to dissipate during the bubbles' free fall.

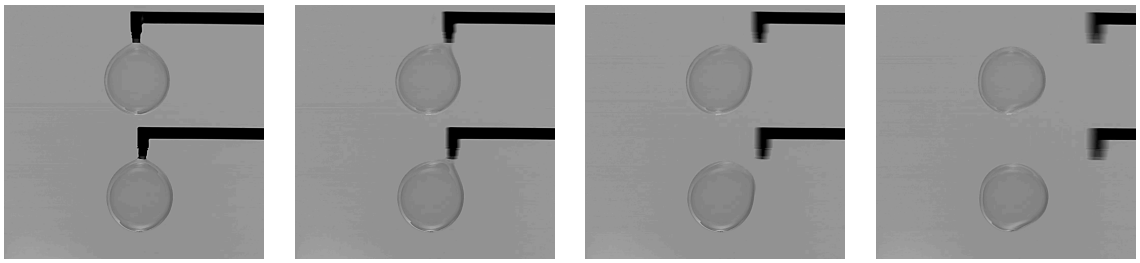

(a) (b) (c) (d)

Figure 3: Initial condition setup for an Ar/Ar bubble pair. (a) Initial retractor position. Time after initiating retraction: (b) 36 ms, (c) 48 ms and (d) 64 ms.

Upon interaction with the shock wave, the bubble soap film atomizes, generating liquid droplets with diameter less than 10 μm. A cross section of the flow is illuminated with a laser sheet and the light deflected by the droplets by Mie scattering is collected onto a CMOS camera. Using a dual-cavity laser and a camera capable of recording two images in very rapid sequence (TSI Powerview 630094) allows to collect two post-shock images per experiment. Initial condition (pre-shock) images are acquired with cameras oriented at 90° from each other, using front and back lighting. A schematic of the diagnostics setup is shown in Fig. 4 while examples of these images are shown in Figs. 5.

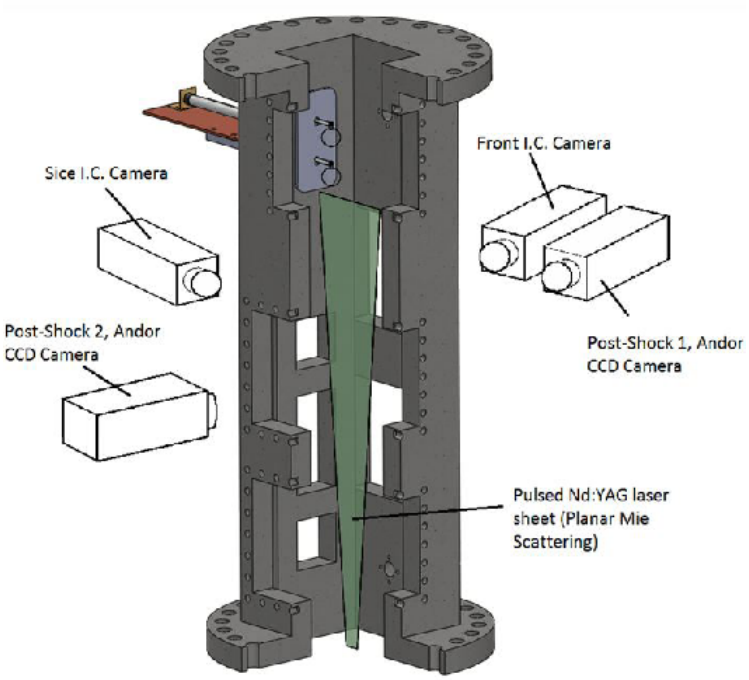

Figure 4: Schematic view of the diagnostic setup.

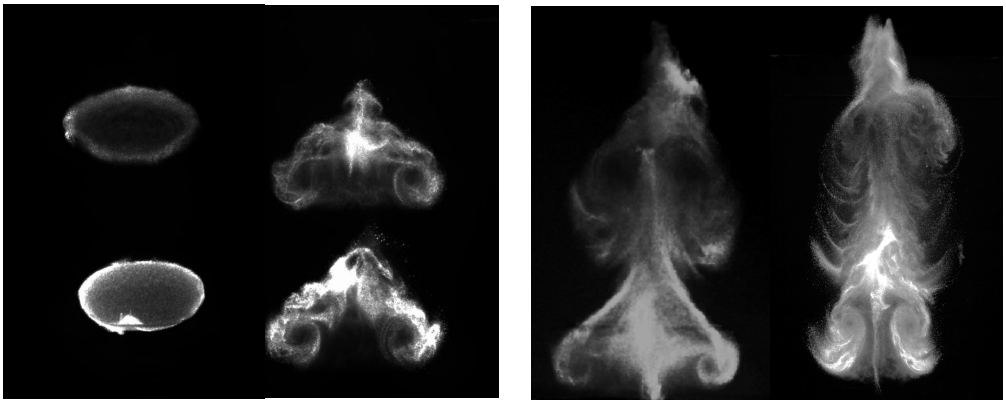

(a) (b) (c) (d)

Figure 5: Left: Ar-Ar bubble pair accelerated by a M=1.47 shock wave. (a) 466 μs; (b) 1.636 ms. Right: Xe-Ar bubble pair accelerated by a M=1.47 shock wave. (c) 644 μs; (d) 1.814 ms.

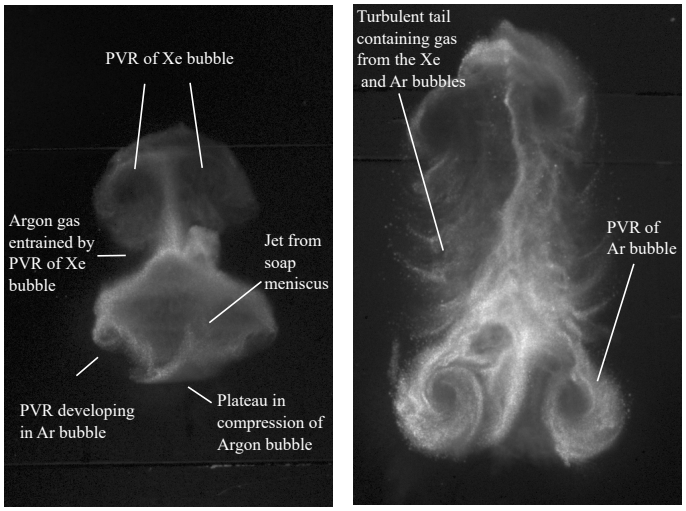

Figure 6: Details of post-shock Xe-Ar pair: (a) t=0.5 ms; (b) t=1.5 ms.

In the Ar-Ar case, the two bubbles have the same diameter when they separate from the injector and, having the same mass, they fall at the same speed, thus maintaining their initial separation (about one bubble diameter). The post shock images indicate that there is essentially no interaction between the bubbles and that each evolves very similarly to a single shock-accelerated bubble (Fig.5(a) and (b)).

Significant interaction between the two bubbles takes place in the Xe-Ar case (Fig.5(c) and (d)). The Xe bubble is the upper one. Since the density of xenon is 3.28 times that of argon, and because of the limits imposed by the soap surface tension, when the bubbles separate from the injectors the xenon bubble has a diameter about half the diameter of the argon bubble. Furthermore, the Xe bubble falls at a higher speed than the Ar bubble, causing the two bubbles to be in contact with each other by the time the shock wave accelerates them. Actually, control of the initial conditions in the Xe-Ar case is extremely difficult and the two bubbles often do not fall along the same vertical line.

Details of the strong interaction between the bubbles, with the stretched top of the bottom bubble penetrating into the main vortex ring of the top bubble can be seen *e.g.* in Fig. 6. Figure 6(a) shows the early direct interaction of the two bubbles, with an entrainment of the argon gas caused by the primary vortex ring (PVR) of the xenon bubble. The second post-shock image (Fig. 6(b)) shows the well-developed vortical structures in both bubbles and a turbulent tail that connects the two gases.

The physics at play can be understood with the aid of the sketches shown in Figs. 7-9. Initially, the planar shock wave will interact with the upper bubble as if it were a single bubble case, shown in Figs. 7(a)-(c). As seen in Figs. 7(d), however, the presence of a second inhomogeneity becomes significant. The compression of the ambient gas that is between the two bubbles causes the inhomogeneities to be closer to each other. The incident wave that has fully traversed the upper bubble collides with the lower bubble leaving behind a reflected shock wave that moves towards the upper bubble. This reflected shock wave, without much delay, interacts with the downstream end of the upper bubble as seen in Fig. 8(a), sending a convex reflected wave, green in the figure, back towards the lower bubble. Unlike the incident shock wave, which is nearly flat by the time it collides with the lower bubble and is shown as a solid red line in the figure, the curvature of the reflected shock wave shown in Fig. 8(a) causes a larger deposition of local vorticity on the upstream side of the lower bubble.

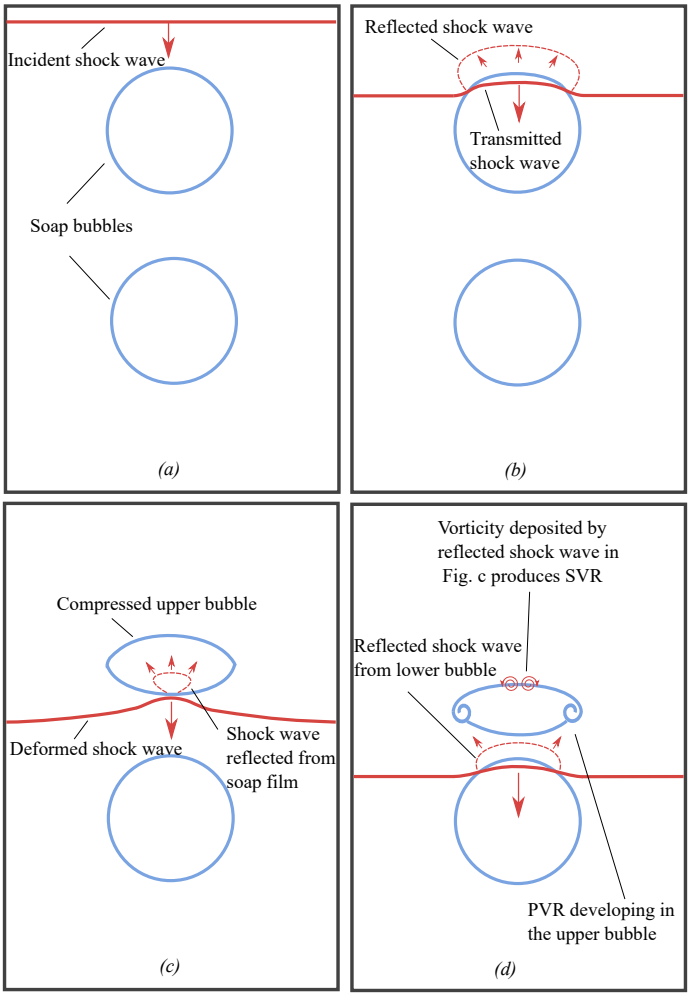

Figure 7: Early stages of the interaction of a planar shock with two bubbles.

This is mainly due to the fact that the shock wave reflected from the upper bubble has an opposite curvature than the lower bubble. Fig. 8(b) shows the baroclinic vorticity deposited by the concave reflected shock wave. Even though the upper bubble interacts with multiple reflected waves, the deposition of vorticity is relatively weak due to curvature. Finally, the incident shock wave that has transmitted through the lower bubble produces another reflected shock wave, shown in Fig. 8(c). This reflected wave is the equivalent of the main producer of the secondary vortex ring (SVR) for a single bubble case. The interaction of this reflected wave, shown red in Fig. 8(c), with the upstream side of the lower bubble deposits additional vorticity in the area that develops into a SVR at later times. Additional shock wave reflections and interactions continue to occur as the bubbles travel down the shock tube. They are, however, weak compared to those shown in Figs. 7-8 due to dissipative effects.

For the case of a Xe-Ar pair, in most cases examined in this study, the proximity of the two bubbles causes the diffracted portion of the wave that is traveling around the xenon bubble to collide the argon bubble before the wave fully traverses the xenon bubble. The large acoustic impedance mismatch will cause this diffracted wave to bend dramatically as it approaches the shock focusing point at the downstream pole of the upper bubble, shown in Fig. 9(c).

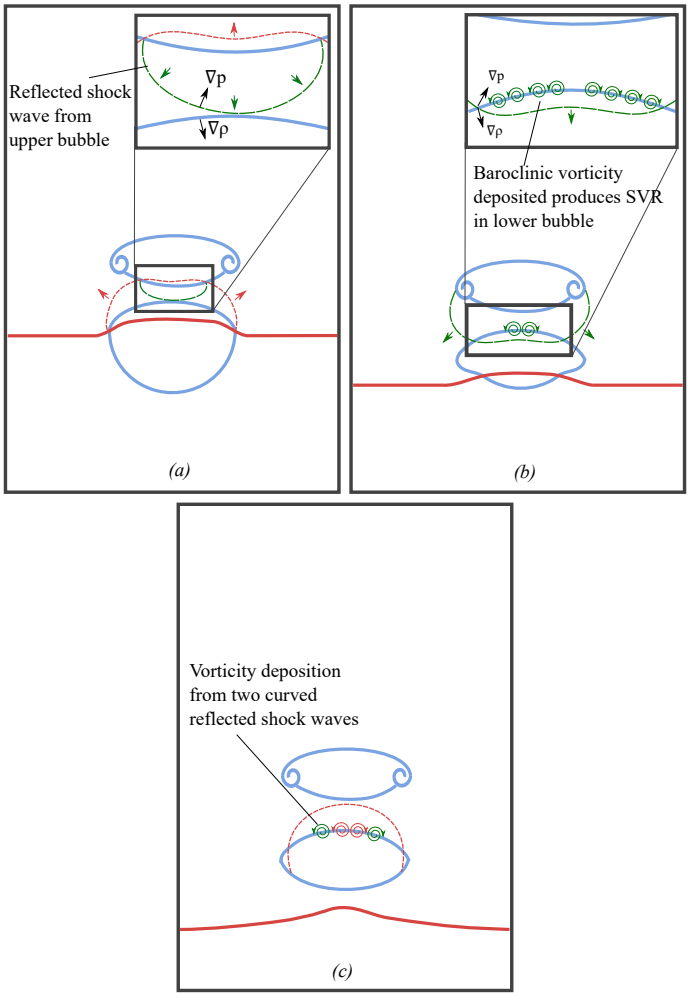

Figure 8: Late stages of the interaction of a planar shock with two bubbles.

The large curvature of the diffracted wave that collides with the argon bubble causes a compression in the direction shown by the blue arrows in Fig. 9(c). As opposed to the oval shaped compression seen in the single and dual bubble argon experiments, this leads to the diamond-like shape that is displayed by the lower bubble in Fig. 6(a). The downstream pole of the shocked bubble also shows this kind of compression, with a plateau at the center. The diamond-like compression downstream is likely due to the wave that is reflected from the shock focusing point as shown in Fig. 9(d).

The digital images are analyzed to extract macroscopic dimensions like lateral and axial extent, and vortex ring minor and major diameters. Specifically, pixel value lineouts are used to identify the boundaries of the shocked bubbles. Examples of these lineouts are given in Fig. 10.

The lengths extracted from the digital images are normalized using the appropriate pre-shock bubble diameter, D_0; time, t, is normalized using $\tau = \frac{2tW_t}{D}$, where W_t is the velocity of the shock wave transmitted into the bubble (estimated from 1-D gasdynamics). The normalized width, W, and axial extent, H, will be indicated below with L_W and L_H, respectively. The results are shown in Figs. 11-13 and compared to previous results by Ranjan [3–5] and Haehn [6].

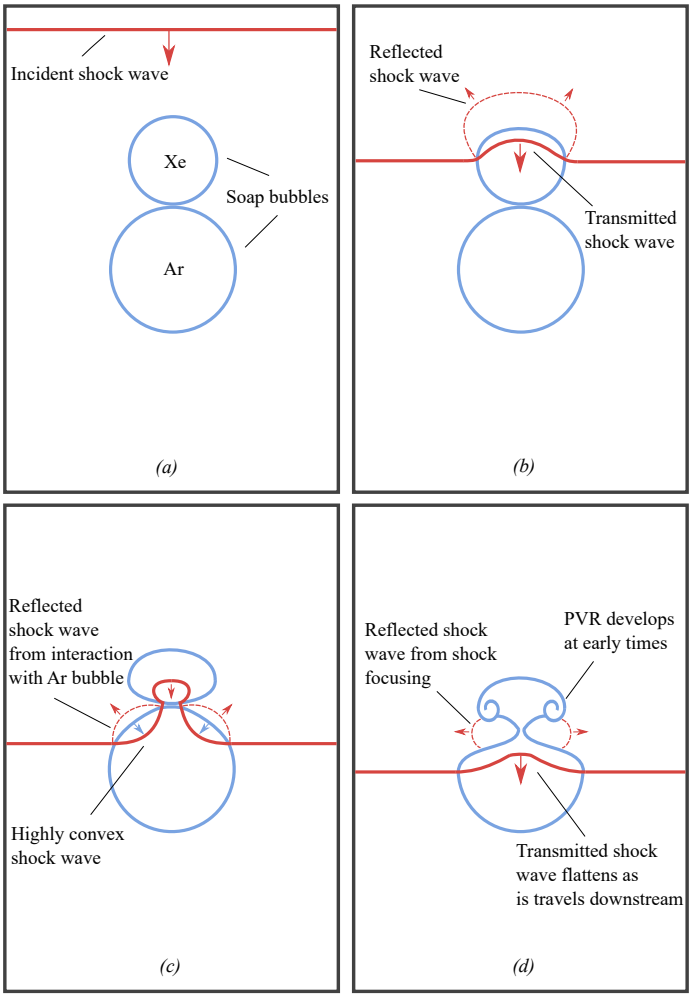

Figure 9: Stages of the interaction of a planar shock with a Xe-Ar bubble pair.

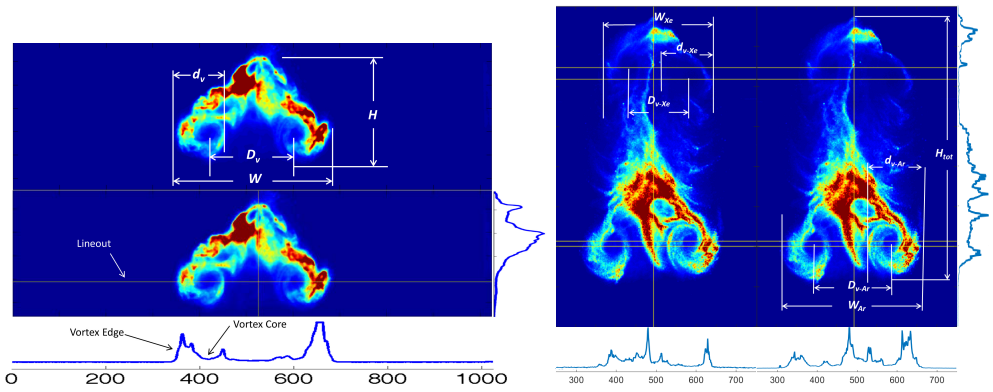

Figure 10: Pixel value lineouts. Left: lineouts for the top bubble in an Ar-Ar pair. Right: lineouts for an entire Xe-Ar pair.

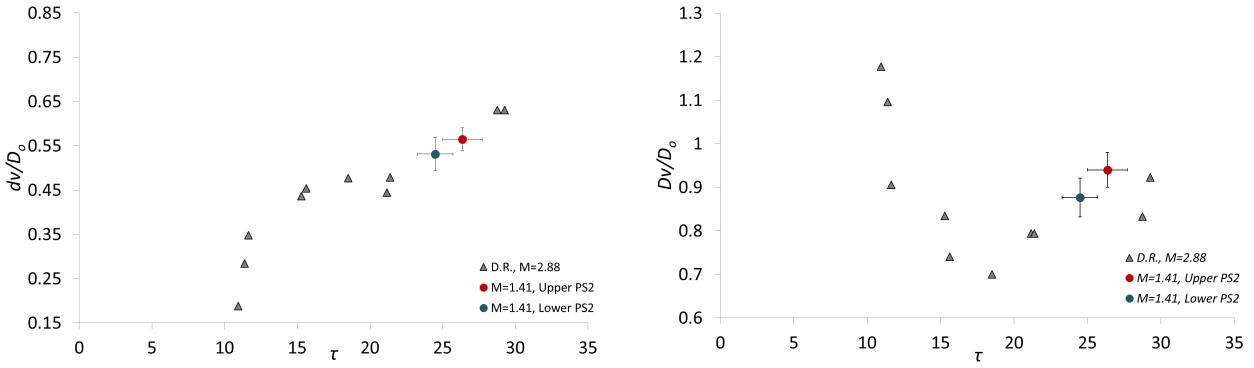

Figure 11: Ar-Ar pair diameters. Left: core diameter. Right: inner ring diameter. D.R. indicates Devesh Ranjan's data [3–5].

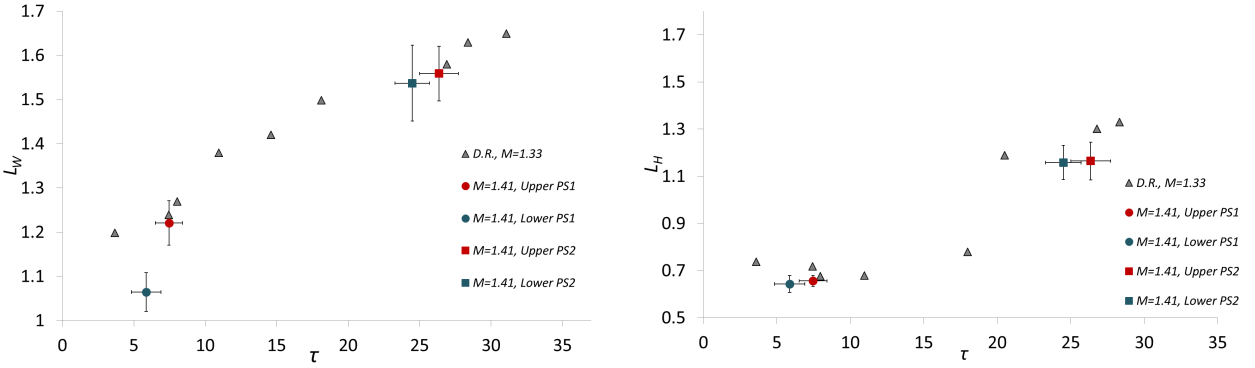

Figure 12: Ar-Ar pair dimensions. Left: outer ring diameter. Right: axial extent. D.R. indicates Devesh Ranjan's data [3–5].

It can be seen (Figs. 11 and 12) that the bubbles in the Ar-Ar pair behave very similarly to the single bubbles studied by Ranjan and Haehn, *i.e.* the second bubble does not affect the first bubble much at all. On the other hand (Fig. 13) the xenon bubble displays a significantly larger value at the early post-shock times. This is an effect of the normalization used, *viz.* the use of the transmitted shock wave speed W_t in the definition of the dimensionless time τ, and the significantly larger deposition of vorticity that accompanies the larger density gradient experienced in a nitrogen-xenon interface. The much larger Atwood number for the xenon/nitrogen pair results in a transmitted shock wave that is significantly slower than its predecessor. The values at the second post-shock time separate significantly from the trend displayed by the single bubble case. At this time, there is a very complex, direct interaction between the two bubbles. The argon bubble experiences a decrease in its lateral growth rate. One of the key features involving the interaction between the two bubble gases is the entrainment of argon gas by the xenon primary vortex ring. This entrainment causes an elongation of the bubble gas at the expense of the lateral growth, hence the results obtained.

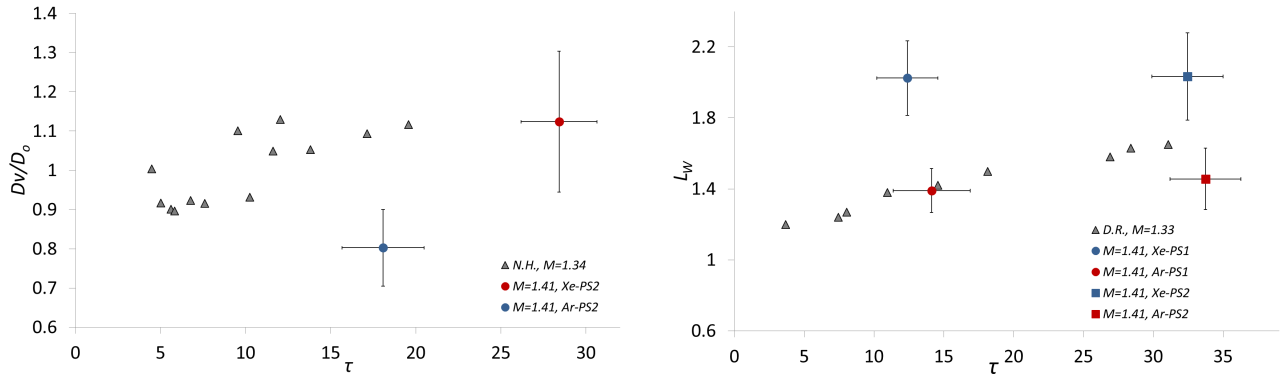

Figure 13: Xe-Ar pair dimensions. Left: inner ring diameters. Right: outer ring diameters. N.H. indicates Nick Haehn's data [6]. D.R. indicates Devesh Ranjan's data [3–5].

4 Numerical simulations

4.1 Simulations of shock tube experiments

We complement the laboratory experiments of SAIF with multiple bubbles conducted at the Wisconsin Shock tube Laboratory (WiSTL) described above with tailored simulations that replicate the laboratory setup.

Results from our matched 2D Flash simulations reproduce the salient features from the experiment, as shown in Fig.14 and thus serve as both validation for the fidelity of the hydro code and as a diagnostic tool for studying the laboratory experiment, in that hydro quantities that are hard to assess in the experiment (3D velocity fields, chemical mixing, temperature and entropy, etc.) can be readily determined from the computational grid.

The good agreement with the experiment supports the use of both tools to study SAIFs: Laboratory experiments can explore flows without numerical resolution limits (which generally impose unphysical numerical viscosity on the problem), while simulations like the ones performed in this study can explore parameter regimes inaccessible to experiments, such as (a) high Mach numbers, (b) magnetized flows, (c) complex geometries, such as filamentary density inhomogeneities.

4.1.1 Magnetohydrodynamic simulations of shock bubble interactions

A critical aspect of astrophysical SAIFs is the magnetization of the fluid. For example, in the case of galaxy clusters, where large scale shocks excited either by the action of supermassive black holes in the center of the cluster or from so-called merger shocks (due to the dynamical interaction of two galaxy clusters) or from cluster accretion shocks, *both* the intracluster medium *and* the bubbles (relativistic plasma inflated by relativistic outflows from the vicinity of the central black hole seen as so-called radio lobes) are magnetized, though at different relative and absolute field strengths.

A major goal of our work is to study and understand the impact of magnetic fields on SAIF in the context

of clusters. This study cannot be performed experimentally at the current time. However, we can use numerical simulations that are calibrated to the laboratory results in the hydrodynamic limit and impose an initial magnetization of the fluid, following the development of SAIF in the magneto-hydrodynamic limit.

To this end, we developed a suite of `FLASH`4.2 [1] simulations of interaction of shock waves with magnetized fluids. Simulations were performed using the unsplit staggered-mesh magneto-hydrodynamic (MHD) solver implemented in FLASH [7], which solves the MHD equations using the so-called constrained transport prescription.

In a previous study [8], we investigated the interaction of waves with magnetized fluids where the magnetic field is *highly ordered* (*i.e.* homogeneous), showing that magnetized fluids can, in principle, strongly affect the development of vorticity in SAIFs.

However, the large scale fields in galaxy clusters and inside radio lobes are *tangled* on scales smaller than the size of the system, unlike the study performed by [8]. We performed a series of simulations to investigate the effects of tangled magnetic fields on the development of the Richtmyer-Meshkov instability (RMI) in shock-bubble interactions.

Initial conditions were generated using a Gaussian random-phase magnetic vector potential with a preselected power spectrum (such that most power is at relatively large scales), satisfying the solenoidal condition on the magnetic field. The power spectrum is of the form

$$\vec{B}_k \cdot \vec{B}_k^* \propto k^{-2.5} \exp\left[-\left(\frac{k}{k_1}\right)^2\right] \exp\left[-\frac{k_2}{k}\right] \tag{1}$$

and wave numbers k, $k_1 = 16$ and $k_2 = 0.5$ are measured relative to the radius of the bubble. The magnetic topology for a given power spectrum is further varied by changing the initial random seed used to generated the vector potential.

We investigated fields isolated to the bubble, fields that span the entire computational domain (*i.e.* both the bubble interior and the exterior), and fields that are ordered on scales larger than the bubble, similar to the study in [8] but with the bubble magnetically isolated from the surroundings, such that the magnetic field lines are draping the bubble. An example volume rendering of an isolated bubble simulation (*i.e.* zero field in the external gas) is shown in Fig. 15.

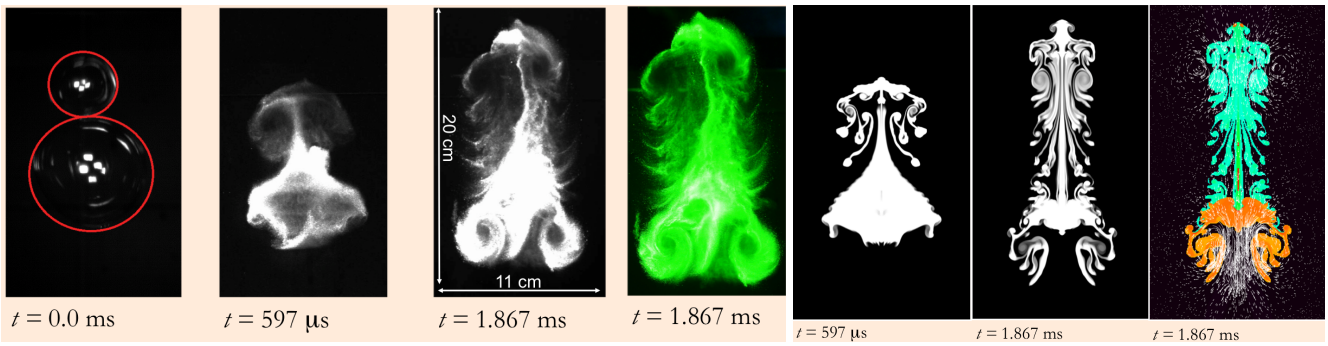

Figure 14: *Left:* Experimental data: Planar Mie Scattering Images of a shock interacting with two bubbles — one xenon and one argon bubble — shown at four different times. *Right:* Simulation of the experiment shown as a density slice through the central plane of the simulation.

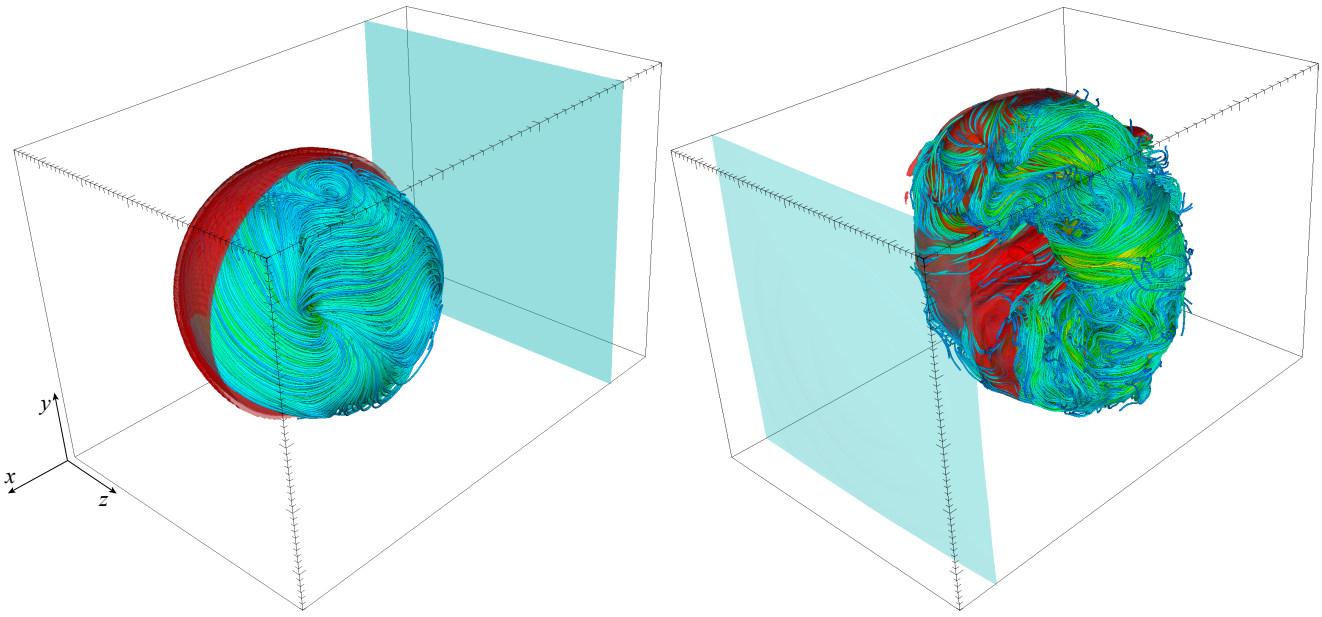

Figure 15: *Left:* 3D rendered image of the initial conditions of a magnetize SAIF simulation (run 128-beta 1 in Tab. 1); shown are an iso-density contour (red surface) restricted to the $y < 0$ domain, the shock (cyan surface) traveling in the $+x$ direction, and tangled magnetic field lines, isolated to the interior of the bubble; *right:* the same simulation after shock passage, showing the generation of the usual vortex ring and the shear-amplified magnetic field restricted to the torus due to magnetic flux-freezing.

We performed a series of simulations of different magnetic field topologies and field strengths, listed in Table 1. Simulations were run on the University of Wisconsin Advanced Computing Initiative cluster. A typical simulation would run on 80 cores for about 10 days. Overall, we used roughly 200,000 CPU hours.

Given the density contrast typically found in SAIFs in galaxy cluster environments, we limited our investigation to cases where the bubble is significantly less dense than the surrounding medium, with an Atwood number of $\frac{\rho_{\rm ISM} - \rho_{\rm bubb}}{\rho_{\rm ISM} + \rho_{\rm bubb}} = 0.99$.

Figure 15 shows a before- and after 3D rendered image of the magnetic fields in the bubble.

In order to quantify the impact of magnetization on the development of the RMI, we extracted the solenoidal kinetic energy (vortex energy) from the flow by performing a Helmholtz decomposition of the velocity field, similar to [9, 10].

We define the plasma beta parameter as the usual ratio of gas pressure to magnetic pressure, $\beta \equiv p_{\rm gas}/p_{\rm B} = p_{\rm gas}/(B^2/8\pi)$.

Main result: We find that the impact of magnetization depends strongly on field topology: If the field is isolated to the low-density interior of the bubble, the impact on the development of the RMI is moderate: Even in the strongly magnetized case of $\beta \sim 1$ (*i.e.* the case where the field is dynamically important for the interior), the energy deposited into the vortex is reduced by approximately a few percent only.

On the other hand, in the case where the *entire* computational domain is magnetized, the effects of even *weak* fields are significant: For example, in the case of $\beta \sim 100$ (*i.e.* gas pressure 100 times larger than magnetic pressure) the field suppresses the energy in the vortex by approximately 50%.

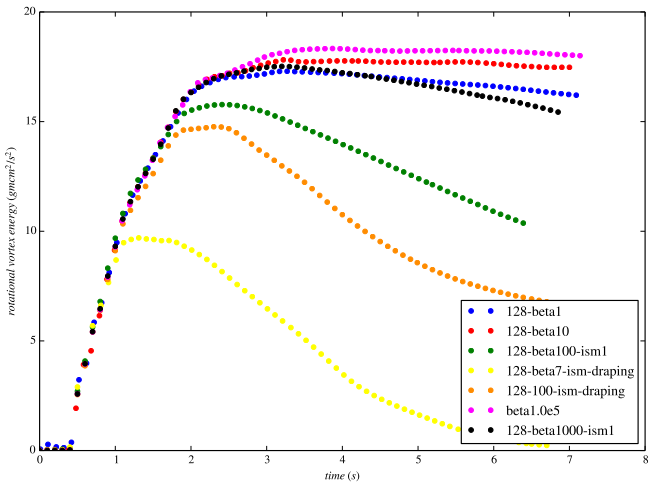

Figure 16: Plot of vortex energy as a function of time for three magnetic field topologies and different magnetic field strengths: Strong field isolated within the bubble (blue, $\beta = 1$), moderate field isolated within the bubble (red, $\beta = 10$), hydro case (magenta, $\beta = 10^{-5}$), weak tangled field throughout the domain (green, $\beta = 100$), very weak tangled field throughout the domain (black, $\beta = 1000$), strong ordered magnetid field in draping topology (yellow, $\beta = 7$), weak ordered magnetic field in draping topology (orange $\beta = 100$). While a strong field restricted to the interior of the bubble has little effect on the development of the vortex (blue), even a weak field that permeates the external medium can strongly suppress the vortex (green).

Simulations					
Name	Resolution	β	Topology	ISM Magnetized	Seed
128-beta1	128	1	Isolated	No	Seed1
128-beta10	128	10	Isolated	No	Seed1
128-seed2	128	1	Isolated	No	Seed2
64-beta1	64	1	Isolated	No	Seed1
32-beta1	32	1	Isolated	No	Seed1
16-beta1	16	1	Isolated	No	Seed1
128-beta1-ism1	128	1	Isolated	Yes	Seed1
128-beta100-ism1	128	100	Isolated	Yes	Seed1
128-beta100-ism2	128	100	Continuous	Yes	Seed1
128-beta100-ism2	128	7	Continous	Yes	Seed1

Table 1: Table of simulation parameters for MHD simulations of SAIFs. Resolution denoted in computational cells across bubble; plasma β parameter denotes the ratio of gas pressure to magnetic pressure

This can be seen in Fig. 16 which plots the solenoidal energy in the case an unmagnetized exterior and strongly (blue) or weakly (red) magnetized bubble (blue), compared to the case of a uniformly but weakly magnetized domain (green).

We can interpret this effect in the context of ideal MHD: the magnetic field in the exterior medium acts like a source of large scale stress, *i.e.* as a spring that winds up as the flow rotates, suppressing the generation of vorticity. This is similar to the role magnetic fields play in the formation of the Kelvin-Helmholtz instability [11], where $\vec{B}$ acts like an effective surface tension.

Magnetization of this gas is more effective in suppressing the deposition of energy into the vortex flow.

Because the characteristic velocities of the fluids inside and outside of the bubble are similar (of the order of the shock velocity), the bulk of the vortex energy is located in the dense external gas. Because most of the vortex energy is in the *external* medium, the fields inside the low-density bubble have little effect on the formation of the vortex, while even moderate fields in the external medium will be shear-amplified by the formation of the vortex to become dynamically important.

5 Conclusions

The release of a train of two bubbles in free fall inside the shock tube proved to be an extremely difficult task. Because the top bubbles travels within the wake of the bottom one, its motion is quite erratic with significant two-dimensional oscillations about a vertical trajectory. It is impossible to ensure that the two bubbles will fall along the same vertical line. Nevertheless, quantitative data were successfully gathered from several experimental series and compared against those for the single bubble case.

6 Products

Conference presentations include:

"Shock- acceleration of a pair of gas inhomogeneities", G. Wattal, A. Navarro Nunez, D. Reese, J. Oakley, D. Rothamer, S. Heinz, R. Bonazza, 14th International Workshop on the Physics of Compressible Turbulent Mixing, San Francisco, CA, September 2014.

"A numerical investigation of the Richtmyer-Meshkov induced vorticity in the multi-phase interstellar medium", G. Wattal, S. Heinz, R. Bonazza, J. Oakley, 67th Annual Meeting of the Division of Fluid Dynamics of the American Physical Society, San Francisco, CA, November 2014.

"Shock-acceleration of a pair of gas inhomogeneities", J.A. Navarro Nunez, D. Reese, J. Oakley, D. Rothamer, R. Bonazza, 67th Annual Meeting of the Division of Fluid Dynamics of the American Physical Society, San Francisco, CA, November 2014.

"Shock Bubble Interactions in the Intra-cluster Medium" G. Wattal, S. Heinz, Princeton Prospects in Theoretical Physics, July 2016;

"All Curled Up: Shock-Accelerated Inhomogeneous Flows in the ICM", S. Heinz, G. Wattal, E. Churazov, R. Bonazza, J. Oakley, invited talk at the Physics of the Intracluster Medium Workshop, Minneapolis, MN, August 2016 (slides available at http://conservancy.umn.edu/handle/11299/182029).

Mr. Alonso Navarro completed his M.S. thesis entitled "Experimental Investigation of the Shock-bubble Interaction with Two Spherical Inhomogeneities" in December 2015.

A comprehensive journal article is currently being written for submittal to Astrophysical Journal.

7 Participants

Undergraduate students: Alex Ames, Mitchell Corcoran, Chris Noble, Gunnar Thompson, Dylan Vann.

Graduate students: Alonso Navarro, Gandhari Wattal, Chris Noble, Dan Reese.

Scientist: Jason Oakley.

Faculty: Riccardo Bonazza, Dave Rothamer, Sebastian Heinz.

References

[1] B. Fryxell, K. Olson, P. Ricker, F. X. Timmes, M. Zingale, D. Q. Lamb, P. MacNeice, R. Rosner, J. W. Truran, and H. Tufo. FLASH: An Adaptive Mesh Hydrodynamics Code for Modeling Astrophysical Thermonuclear Flashes. *Astrophysical Journal Supplements*, 131:273–334, November 2000.

[2] M H Anderson, B P Puranik, J G Oakley, P W Brooks, and R Bonazza. Shock tube investigation of hydrodynamic issues related to inertial confinement fusion. *Shock Waves*, 10(5):377–387, November 2000.

[3] Devesh Ranjan, Mark Anderson, Jason Oakley, and Riccardo Bonazza. Experimental Investigation of a Strongly Shocked Gas Bubble. *Physical Review Letters*, 94(18), May 2005.

[4] D Ranjan, J Niederhaus, B Motl, M Anderson, J Oakley, and R Bonazza. Experimental investigation of primary and secondary features in high-Mach-number shock-bubble interaction. *Physical Review Letters*, 98:024502, January 2007.

[5] John H J Niederhaus, J A Greenough, J G Oakley, D Ranjan, M H Anderson, and R Bonazza. A computational parameter study for the three-dimensional shock–bubble interaction. *Journal of Fluid Mechanics*, 594(-1):85–124, December 2007.

[6] Nicholas Haehn, Devesh Ranjan, Chris Weber, Jason Oakley, David Rothamer, and Riccardo Bonazza. Combustion and Flame. *Combustion and Flame*, 159(3):1339–1350, March 2012.

[7] D. Lee, A. E. Deane, and C. Federrath. A New Multidimensional Unsplit MHD Solver in FLASH3. In N. V. Pogorelov, E. Audit, P. Colella, and G. P. Zank, editors, *Numerical Modeling of Space Plasma Flows: ASTRONUM-2008*, volume 406 of *Astronomical Society of the Pacific Conference Series*, page 243, April 2009.

[8] S. H. Friedman. *All Curled Up: The Hydrodynamics of Vortex Rings in Galaxy Clusters by Way of Helmholtz Decomposition*. PhD thesis, UNIVERSITY OF WISCONSIN-MADISON, 2011.

[9] S. Heinz and E. Churazov. Heating the Bubbly Gas of Galaxy Clusters with Weak Shocks and Sound Waves. *Astrophysical Journal Letters*, 634:L141–L144, December 2005.

[10] S. H. Friedman, S. Heinz, and E. Churazov. All Curled up: A Numerical Investigation of Shock-Bubble Interactions and the Role of Vortices in Heating Galaxy Clusters. *Astrophysical Journal*, 746:112, February 2012.

[11] S. Chandrasekhar. *Hydrodynamic and hydromagnetic stability*. Clarendon, 1961.